



Role of oxygen vacancies and Mn sites in hierarchical $\text{Mn}_2\text{O}_3/\text{LaMnO}_{3-\delta}$ perovskite composites for aqueous organic pollutants decontamination

Yuxian Wang^{a,b}, Lulu Chen^a, Hongbin Cao^b, Zhaoxu Chi^a, Chunmao Chen^a, Xiaoguang Duan^c, Yongbing Xie^{b,*}, Fei Qi^d, Weiyu Song^a, Jian Liu^{a,*}, Shaobin Wang^c

^a State Key Laboratory of Heavy Oil Processing, China University of Petroleum-Beijing, 18 Fuxue Road, Beijing, 102249, China

^b Division of Environment Technology and Engineering, Institute of Process Engineering, Chinese Academy of Sciences, Beijing, 100190, China

^c School of Chemical Engineering, The University of Adelaide, Adelaide, SA 5005, Australia

^d Beijing Key Lab for Source Control Technology of Water Pollution, College of Environmental Science and Engineering, Beijing Forestry University, Beijing, 100083, China



ARTICLE INFO

Keywords:

Perovskites
Catalytic ozonation
Oxygen vacancies
Density functional theory
Reactive oxygen species

ABSTRACT

La-based perovskites are catalytically active owing to the oxygen vacancies, redox metal centers of B sites and surface hydroxyl groups. Nevertheless, the insights into these active centers on environmental catalysis are still insufficient. In this study, hierarchical mixed oxides perovskite microspheres were synthesized for catalytic ozonation over oxalic acid and benzotriazole. LaMn_4O_x , with $\text{LaMnO}_{3-\delta}$ as the dominant crystal phase, demonstrated superior catalytic activity to Mn_2O_3 and LaMnO_3 synthesized from citric acid sol-gel method. Temperature-programmed desorption of NH_3 (NH_3 -TPD) and pyridine-Fourier transform infrared spectroscopy (pyridine-FTIR) tests proved Lewis acid as the main acid type. Temperature-programmed reduction of H_2 (H_2 -TPR), O_2 -TPD and X-ray photoelectron spectroscopy (XPS) analysis indicated the presence of oxygen vacancies and mixed valences of Mn in the crystal structure facilitated the catalytic process. Moreover, the content of oxygen vacancy was calculated by iodometric titration method. With the aid of theoretical calculations, oxygen vacancies were found to exhibit a strong affinity toward ozone adsorption, where ozone molecules spontaneously dissociated into reactive oxygen species (ROS) such as $\text{O}_2^{\cdot-}$ and ${}^1\text{O}_2$. The B site of Mn facilitated ozone decomposition by extending the O–O bond of ozone due to the electron transfer from $\text{Mn}^{3+}/\text{Mn}^{4+}$ redox cycle. In-situ EPR and quenching tests confirmed the contribution of $\text{O}_2^{\cdot-}$ and ${}^1\text{O}_2$ in benzotriazole degradation along with ${}^{\cdot}\text{OH}$. This study stepped further to unveil the ozone adsorption/decomposition and ROS generation on nanoscale perovskite-based composites.

1. Introduction

Perovskites featured with a nominal structure of ABO_3 have emerged as attractive candidates for heterogeneous catalysis [1–3]. Great flexibility of perovskites' structure and composition has been achieved by their capability of bearing most of the metal elements, which in turn manipulates the catalytic performances in diverse catalytic reactions [4]. Meanwhile, it is feasible to tune the physicochemical and electronic properties by rational substitution of A and/or B cations and regulating the proportion of chemical components [5,6]. Extensive studies have reported the utilization of lanthanides cations as A site metal owing to their singular crystal structures that facilitate the exposure of B site metal cations without compromising in catalytic activity [7,8]. On the other hand, B sites are critical for modifying the catalytic performances of perovskites. Together with A sites, a large

population of defective sites such as oxygen vacancies could be induced [9]. Moreover, metal cations hosted in B sites with stable mixed valence states are favorable for electron transfer with high redox behavior [10,11]. Manganese cation have been broadly employed as B site metal in perovskites due to their variable valence states and low toxicity to the environment [12,13]. Meanwhile, the activity of shape-controlled manganese oxides originating from the interlinked edge-sharing MnO_6 octahedral provides a platform for exploring the facet-performance chemistry and structural effects in heterogeneous catalysis [14]. Recently, efforts have been dedicated to investigating the catalytic reactivity of lanthanum manganite perovskites (LMO) in energy conversion and environmental remediation [15,16]. For crystalline materials at nanoscale, defective sites could exert a profound effect on the physicochemical properties and the formation of which would tailor the surface morphology and electronic structure to improve their catalytic

* Corresponding authors.

E-mail addresses: ybxie@ipe.ac.cn (Y. Xie), liujian@cup.edu.cn (J. Liu).

activities [17]. Among these structure defects, oxygen vacancies on the surface of the metal oxides obtain a pronounced catalytic potential [5,9,18]. The steady chemical bond between metal cation and the adsorbed O₃ on the oxygen vacancy sites would result in the stretch of the O–O bond, which consequently favors the activation or even catalytic dissociation of O₃ molecules for the formation of ROS [19].

Heterocyclic benzotriazoles with fused benzene and triazole rings are widely used as corrosion inhibitors, anti-icing chemicals and dishwasher detergents, which have been discharged from industries and households and accumulated in water systems [20]. Considering their carcinogenicity and toxicity to aquatic organisms and estrogenic activities [21], it is highly imperative to advance efficient technologies for complete mineralization of benzotriazoles. The recent-developed advanced oxidation processes (AOPs) employing reactive species with high redox potentials deliver a complete destruction strategy of these persistent organic pollutants (POPs) with high efficacy [22,23].

Among AOPs, ozonation is favorable for attacking the POPs with unsaturated bonds, but the chemical inertness of O₃ molecules to saturated bonds hinders the further mineralization of the degradation intermediates [24]. On account of the reactive oxygen species (ROS) from ozone activation, catalytic ozonation processes have been evidenced to surpass conventional ozonation by non-selective mineralization of contaminants with high efficiency [25–27]. Apart from hydroxyl radical (·OH), other ROS such as superoxide radicals (O₂^{·-}) and singlet oxygen (¹O₂) can also be produced in catalytic ozonation and contribute to the decomposition of organic pollutants and intermediates [26]. Meanwhile, the pH dependence in ozone decomposition can be rationally regulated by the catalysts, adapting the effectiveness of ozonation to a wider pH range. For catalytic ozonation employing LMO-based perovskites, the variable valence states of Mn offer the electron transfer routes. Previous studies revealed that surface hydroxyl groups and the surface oxygen vacancies of the catalysts can act as Lewis acid sites for accepting electrons [18,28,29]. However, in-depth understanding of the interaction of ozone molecules with these prospective active sites as well as the evolution of the ROS is still insufficient.

Herein, we synthesized a series of LMO perovskites with excessive Mn by a modified co-precipitation method. Hierarchical LMO perovskite composites (LaMn_xO_x) with non-stoichiometric compositions were obtained by tuning the ratio of La and Mn precursors. Oxalic acid (OA) and 1H-benzotriazole (BTA) were utilized as the target pollutants for evaluating the catalytic ozonation activities of the as-synthesized perovskites. The catalytic activity advantage of the LaMn_xO_x over the single component metal oxide (Mn₂O₃) was performed to reveal the potential active sites. Meanwhile, the catalytic activity enhancement brought by the hierarchical structure was investigated by H₂-TPR and O₂-TPD. The average oxidation state (AOS) theory was employed to correlate the activities with actual Mn valence states of the catalysts. Iodometric titration was performed to evaluate the oxygen vacancy content. Density functional theory (DFT) calculations were further performed to probe the mechanistic insights into catalytic ozone decomposition on the potential active sites (oxygen vacancies, metal cations and surface hydroxyl groups) of perovskites. The ROS responsible for BTA degradation were identified by quenching tests and electron paramagnetic resonance (EPR) technique. This study provides a facile approach for the synthesis of shape-controlled LMO and uncovers the in-depth mechanism into catalytic ozone decomposition over perovskite materials.

2. Experimental

2.1. Chemicals and materials

Lanthanum nitrate hexahydrate (99.9%), manganese carbonate (99.9%), ammonium carbonate (99.0%), citric acid (99.9%), oxalic acid (OA, 99.9%), 1H-benzotriazole (BTA, 99.9%), tert-butanol (t-BA,

99.0%) and 2,2,6,6-tetramethyl-4-piperidone (TEMP) were purchased from Aladdin Reagent. Sodium phosphate tribasic (99.5%) and sodium bicarbonate (99.5%) were procured from Sinopharm Chemical Reagent Co. Ltd. Para-benzoquinone (p-BQ, 98.0%) was obtained from Alfa Aesar. Sodium azide (NaN₃, 99.0%) was purchased from Fuchen Chemical Reagent Co. Ltd. 5,5-Dimethyl-1-pyrroline (DMPO) was obtained from Sigma-Aldrich. No further purification was required for these chemicals.

2.2. Synthesis of lanthanum-manganite composites

LMO catalysts with different La/Mn ratios were synthesized via a modified co-precipitation method [14]. Depending upon the molar ratios of the metal precursors employed, the as-obtained materials were denoted as LaMn_{0.5}O_x, LaMnO_x, LaMn₃O_x and LaMn₄O_x, where the La/Mn ratios of the precursors were 1:0.5, 1:1, 1:3 and 1:4, respectively. For comparison, LMO was also synthesized by a reported citric acid sol-gel method and labeled as LaMn₃-C [5]. The detailed synthesis routes of these two methods are demonstrated in Text S1 in supplementary data. Meanwhile, manganese oxide was prepared via a similar co-precipitation protocol without the addition of Mn sources and denoted as Mn₂O₃.

2.3. Characterization methods

The as-prepared catalysts were investigated by N₂ sorption isotherms (Autosorb-iQ, Quantachrome), X-ray diffraction (XRD, PAN analytical B.V., X'Pert-PROMPD), X-ray photoelectron microscopy (XPS, Thermo Fisher Scientific, ESCALAB 50Xi), field emission scanning electron microscopy (FESEM, JEOL, JSM-7001 F), high resolution transmission electron microscopy with energy dispersive X-ray spectrometry (HRTEM with EDX, JEOL 2100 F), pyridine absorbed Fourier transform infrared spectroscopy (FTIR, Bruker, Vortex 70), thermogravimetric analysis (TGA, Mettler Toledo, STAR^e), temperature-programmed desorption by NH₃ and O₂ (NH₃/O₂-TPD, Micrometrics Instrument Corporation, Autochem II 2920), temperature-programmed reduction by H₂ (H₂-TPD, Micrometrics Instrument Corporation, Autochem II 2920) and electron paramagnetic resonance (EPR, Bruker, EMX). Text S2 in supplementary data describes the detailed descriptions of the characterization methods.

2.4. Experimental procedures

Ozonation/catalytic ozonation tests were carried out in a 0.5 L semi-batch reactor submerged in a 25 °C water bath. Ozone was generated from ultrapure oxygen (99.9%) with the inlet flow rate of 100 mL/min and fed from the bottom of the reactor by a glassy porous diffuser. Text S3 in supplementary data illustrates the detailed experiment set-up. The concentration of the target aqueous organic pollutants was monitored by a high-performance liquid chromatography (HPLC, Agilent Series 1260) using a ZORBAX SB-aq C-18 column with the flow rate of 0.25 mL/min. The mobile phases were a mixture of ultrapure water and methanol (60% vs. 40%) and a mixture of diluted phosphate acid solution (2 mM) and methanol (80% vs. 20%) for BTA and OA analysis, respectively. To determine the mineralization rate of the target pollutants, total organic carbon (TOC) was determined on a Shimadzu TOC-vcpb analyzer. To evaluate the stability of the catalyst, the catalyst was recycled after each test by vacuum filtration, washed with ultrapure water for three times, and dried at 80 °C overnight for the next use. The degradation tests were repeated for three times and low deviations (less than 10%) were observed. pH of the solutions was adjusted by 0.01 M NaOH/HCl.

2.5. Theoretical calculation methods

Vienna Ab-initio Simulation Package (VASP) based density

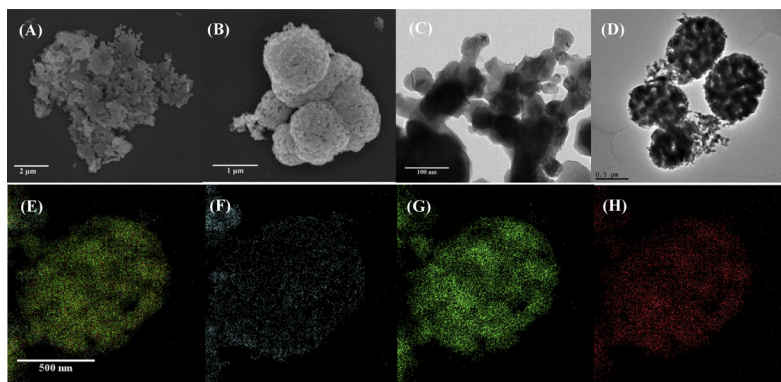


Fig. 1. SEM (A and B) and TEM (C and D) observations of LaMnO_x and LaMn_4O_x , EDX layered graph of LaMn_4O_x (E), EDX mapping on La Mn1 (F), Mn Mn1 (G) and O Mn1 (H).

functional theory (DFT) calculations were performed utilizing projector-augmented-wave (PAW) methods to describe the interactions between atomic cores and valence electrons. The (001) surface of LaMnO_3 with four atomic layers was cleaved for calculation since Mn-terminated surface was more stable than the La-terminated surface [30]. The details of DFT calculations are illustrated in Text S4 in supplementary data.

3. Results and discussion

3.1. Characterization of as-synthesized materials

Morphology of these materials was investigated by SEM and TEM. For LaMnO_x , a highly disordered and agglomerated structure was observed (Fig. 1A). According to XRD analysis, non-stoichiometric $\text{LaMnO}_{3-\delta}$ (JCPDS 86-1228) [31] was identified as the dominant phase for LaMnO_x (Fig. 2A). The other minor peaks observed in the XRD pattern could be ascribed to $\alpha\text{-Mn}_2\text{O}_3$. Interestingly, the disordered structure tended to develop into a rectified shape with the increase of Mn content (Fig. S1), leading to the formation of $\text{Mn}_2\text{O}_3/\text{LaMnO}_{3-\delta}$ composites based on the XRD patterns (Figs. 2A and S2). For LaMn_4O_x , hierarchically clustered microspheres constructed by nanodots were observed with a diameter of around 1 μm (Fig. 1B). Previous study discovered that Ostwald ripening of the agglomerated particles in perovskite formation would contribute to the hierarchical structure [32].

For TEM image of LaMn_4O_x (Fig. 1D), bright crevices were identified within the microsphere structure. Since the formation of the crevices was ascribed to the evaporation of CO_2 from the carbonate precursors during the pyrolysis process, the crevices not only existed on the surface of the catalysts, some of the crevices also penetrated through the hierarchical structure of the catalyst. In HRTEM image (Fig. 2B), crystal lattices with the interplanar spacing of 0.28 nm and 0.23 nm are

observed, which could be indexed to (110) and (202) planes of $\text{LaMnO}_{3-\delta}$, respectively. Moreover, apart from (110) and (202) planes, (104) plane of $\text{LaMnO}_{3-\delta}$ was also identified by the spots on corresponding FFT pattern, which were quite in accordance with the XRD results. According to EDX results (Figs. S4 and 1 E–H), La and Mn were uniformly dispersed within the composite. The atom ratios of La to Mn on LaMnO_x and LaMn_4O_x based on EDX analysis were around 1:1 and 1:2.5, respectively, which is not coincident with that of the precursors, suggesting that not all La and Mn in the precursors were fully taken use of during constructing the spherical structures. TGA results revealed that around 14% of Mn_2O_3 existed in LaMn_4O_x structure (Fig. S5).

3.2. Catalytic ozonation of OA and BTA over perovskite composites

To distinguish the contribution of the generated ROS from ozone, a pilot study was carried out employing oxalic acid (OA, $k_{\text{O}_3} = 0.04 \text{ M}^{-1} \text{ s}^{-1}$, $k_{\text{OH}} = 7.7 \times 10^6 \text{ M}^{-1} \text{ s}^{-1}$) as the target pollutant [33]. Ozonation alone gave rise to less than 10% of OA removal (Fig. 3A), suggesting that insignificant amount of ROS was generated by ozone self-decomposition. In order to provide a benchmark for the catalytic ozonation experiments, adsorption tests were performed. All the catalysts displayed negligible adsorption capabilities for OA removal (< 5%), which might be attributed to the low specific surface areas (SSAs) (Table 1). Moreover, the weak interaction arising from surface charges between catalyst surface and OA molecule might also contribute to the poor physical adsorption. The point of zero charge (pH_{pzc}) value of the LaMn_4O_x was determined to be 7.43 by measuring its zeta potentials under different pHs. With the ambient solution pH of 6.8, the protonated surface of catalyst obtained weak interaction with the un-disassociated OA molecules.

For catalytic ozonation, Mn_2O_3 resulted in the destruction of 90% of initial OA at 60 min and leached Mn ions was 0.4 mg/L. Catalytic ozonation activity of the parent perovskite composite (LaMn_4O_x)

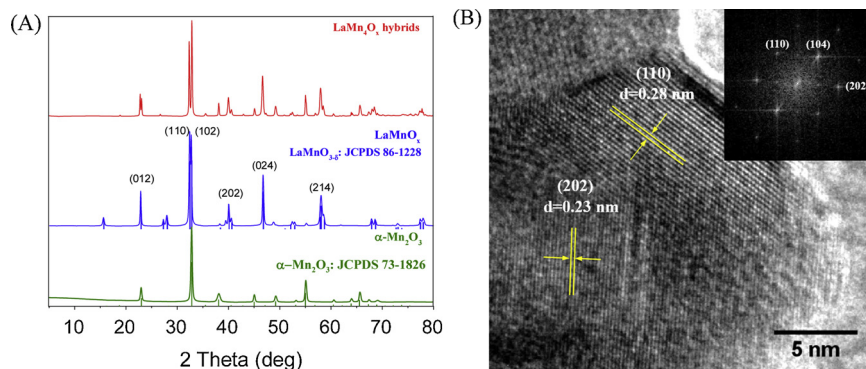


Fig. 2. (A) XRD patterns of as-synthesized materials. (B) HRTEM and the corresponding fast Fourier transform (inset) images of LaMn_4O_x .

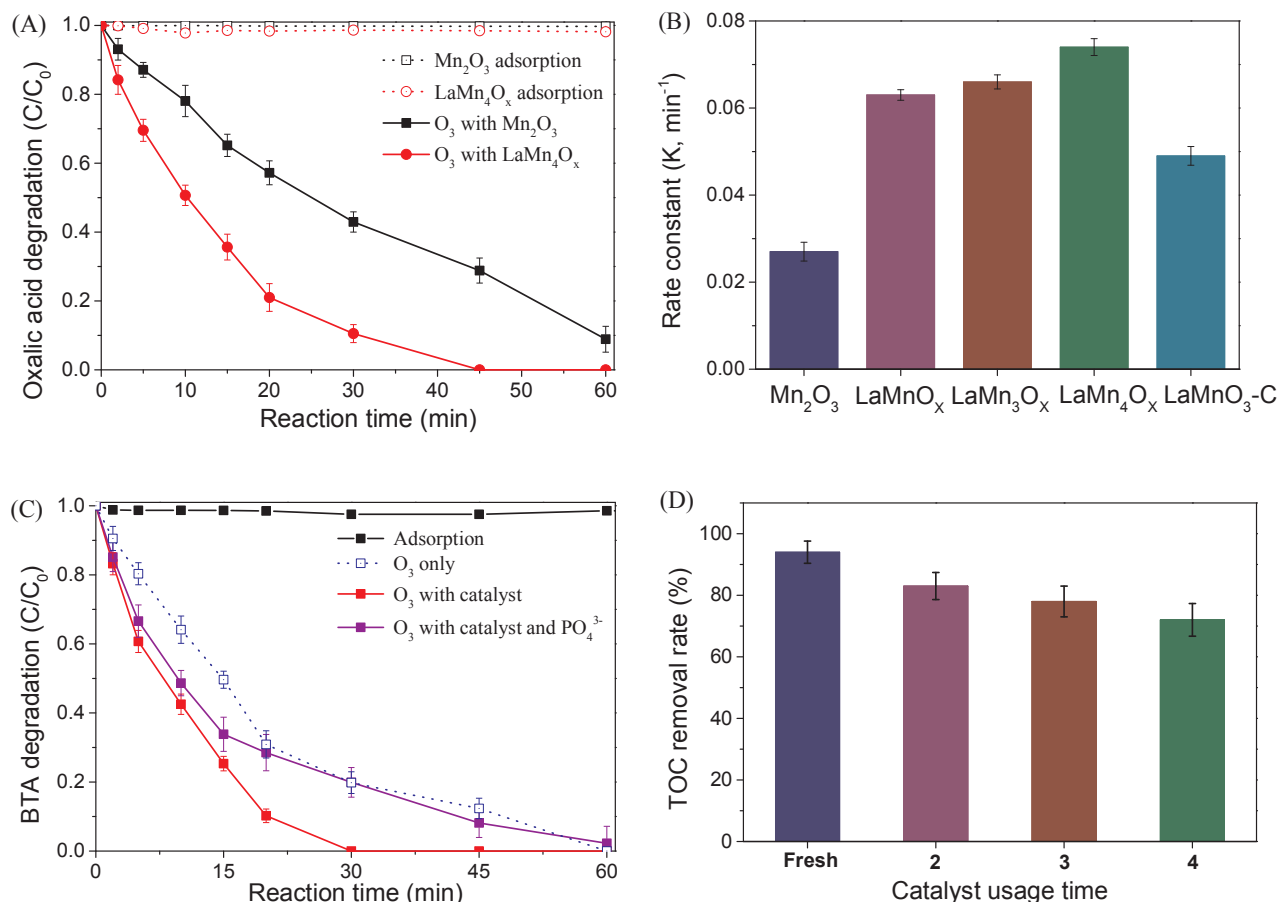


Fig. 3. (A) Oxalic acid removal on different catalysts; (B) Pseudo-first order reaction rate constants of various catalysts for OA degradation; (C) BTA degradation curves on different catalysts and the effect of phosphate anion; (D) TOC removal efficiency on catalyst recycle tests. $[\text{OA}]_0: 50 \text{ mg/L}$; $[\text{BTA}]_0: 50 \text{ mg/L}$; Catalyst loading: 0.2 g/L ; Ozone flow rate: 100 mL/min ; Ozone concentration: 20 mg/L ; Temperature: 25°C ; Initial pH: 6.8. $[\text{PO}_4^{3-}]: 10 \text{ mM}$. pH was adjusted by 0.01 M HCl/NaOH solution.

overwhelmed those of its single composition. Complete destruction of OA was accomplished within 45 min, and less than 0.2 mg/L of Mn ions were detected after 90 min, suggesting a trivial metal loss as well as a minor contribution of homogeneous reaction. Catalytic ozonation activity of LaMn_4O_x also advanced $\text{LaMnO}_3\text{-C}$, for which complete OA decomposition was achieved within 60 min. For a better comparison of the reaction rates, degradation curves were fitted with the pseudo-first-order reaction kinetics (Fig. S7). Fig. 3B displays that LaMn_4O_x obtained a markedly higher rate constant than Mn_2O_3 and $\text{LaMnO}_3\text{-C}$ (0.074 min^{-1} vs. 0.027 and 0.049 min^{-1}).

LMO perovskite composites with different La/Mn ratios were tested in catalytic ozonation for OA decomposition (Fig. S8). As seen, the hierarchical structure favored the catalytic activities of these LMO composites. After 20 min of catalytic reaction, 80% of initial OA was degraded by LaMn_4O_x with the hierarchical structure, whereas LaMnO_x with the agglomerated structure resulted in 70% of OA destruction. The

pseudo-first order reaction rate constants in Table 1 illustrated the activity difference. To further discriminate the catalytic activity enhancement brought by the hierarchical structure, turnover frequency (TOF) was calculated based on OA degradation efficiency and the catalyst's SSA (Text S5 in supplementary data). TOFs of LaMnO_x and LaMn_4O_x were calculated to be 4.0×10^{-3} and $4.4 \times 10^{-3} (\text{m}^2\cdot\text{min})^{-1}$, respectively. Development of hierarchical structure enhanced the TOF. It was speculated that the existence of crevices in the hierarchical structure of LaMn_4O_x would facilitate the exposure of more active sites.

To evaluate the catalytic ozonation efficiency over the unsaturated organic pollutants, 1H-benzotriazole (BTA) with two fused rings (benzene and triazole) was then employed as the target pollutant (Fig. 3C). LaMn_4O_x showed trivial adsorption capability toward BTA, which might be accounted for the low SSAs and aforementioned weak surface interaction forces. Catalytic ozonation led to complete removal of BTA in 30 min. However, BTA degradation efficiency between catalytic

Table 1
Physicochemical properties of as-synthesized materials.

Sample	BET Surface Area (m^2/g)	Pore Volume (cm^3/g)	Rate Constant (min^{-1})	Metal Leaching		Average Oxidation State
				La (mg/L)	Mn (mg/L)	
Mn_2O_3	6.3	0.0089	0.029	–	0.4	3.24
LaMnO_x	9.2	0.016	0.063	0.2	0.2	3.16
LaMn_4O_x	10.4	0.044	0.074	0.1	0.2	3.08
La-Mn-C	11.3	0.028	0.047	0.3	0.3	–
Used LaMn_4O_x	9.8	0.039	0.057	0.1	0.3	3.20

ozonation and ozonation was not distinct since ozone molecules were also effective for BTA degradation. Hereby, TOC removal profiles were crucial to determine the mineralization efficiency. As shown in Fig. S9, with the initial BTA concentration of 25 mg/L, more than 95% of TOC was mineralized by catalytic ozonation, while only 50% of TOC was deducted by ozonation without a catalyst. It is suggested that BTA was predominately removed by ozone, while the generated ROS were responsible for decomposing the intermediates. The reaction solution pH variations further verified the evolution of the degradation intermediates (Fig. S10). For catalytic ozonation, the concave profile of pH variation suggested the production of acidic intermediates which was subsequently mineralized by ROS. For ozonation, however, the solution pH firstly decreased then maintained at a lower value than catalytic ozonation, suggesting the accumulation of the produced acidic intermediates which cannot be further degraded.

To examine the surface properties of perovskites in catalytic reaction, sodium triphosphate (10 mM) was added to the reaction solution (Fig. 3C). As a strong Lewis base, phosphate anion could hinder the interaction between Lewis acid site and ozone molecule [34]. Addition of phosphate anion (10 mM) to catalytic ozonation gave rise to the inhibition of BTA degradation. Complete degradation of BTA was postponed to 60 min with the involvement of phosphate anions. Additionally, the corresponding TOC removal rate decreased from 95% to 62% (Fig. S9). As a strong Lewis base, phosphate anions would impede the ozone adsorption on the Lewis acid sites on catalyst's surface. As seen in Fig. S9, after addition of phosphate anions, the segregation of the surface Lewis acidic sites brought about the inhibition of TOC mineralization efficiency, suggesting the contribution of the surface reactions. However, mineralization of the TOC still occurred in the bulk solution, to which the direct oxidation of the target pollutant/degradation intermediates by ozone molecules and the generated ROS which break away from the catalyst's surface would contribute [34–36].

3.3. Reutilization of LaMn_4O_x

Stability of the LaMn_4O_x was investigated by a four-run successive test (Fig. 3D). Compared with the fresh catalyst, TOC removal rate was decreased to 72% after the fourth run, revealing partial passivation of the catalyst. The decrease in BET specific surface area and corresponding pore volume after usage might be ascribed to the aggregation of catalyst particles and adsorption of degradation intermediates (Table 1). The occurrence of the peaks at 1381 and 1660 cm^{-1} in FTIR spectra revealed the existence of the adsorbed organic intermediates (Fig. S3). On the other hand, a variation of the catalyst surface chemistry properties may also give rise to the passivation. According to the XPS results, the amount of surface Mn^{4+} increased from 28.2 to 34.3% while that of Mn^{3+} decreased from 61.6 to 53.1%, suggesting the partial oxidation of Mn^{3+} cations (Table S2). Though the surface chemistry of LaMn_4O_x was changed, the crystallinity displayed no significant differences as the fresh one (Fig. S2). Metal leaching from the catalyst was also investigated and around 0.3 mg/L of Mn was detected in the solution, this indicated the loss of active Mn cations might be another reason for catalyst deactivation. Nevertheless, homogeneous catalytic ozonation employing filtered reaction solution (after 120 min) resulted in minor contribution of homogeneous reaction (Fig. S9). Our previous study on catalytic ozonation over mesoporous $\alpha\text{-MnO}_2$ also indicated the trivial Mn leaching and the minor effect of homogeneous reaction [37].

3.4. Investigating the potential catalytic active sites

The reduction behaviors of the catalysts were examined by H_2 -TPD experiments (Fig. 4A). Two reduction peaks located in the regions of 200–380 °C and 500–800 °C were observed for the as-synthesized Mn_2O_3 , corresponding to the reduction from Mn_2O_3 to Mn_3O_4 and

Mn_3O_4 to MnO , respectively [38]. For LaMn_4O_x , higher amount of Mn^{3+} gave rise to the shift of the dominant H_2 consumption peak to a higher temperature than Mn_2O_3 , suggesting a lower reducibility. The peak situated in the region 450–640 °C emerged, which might be attributed to the reduction of Mn-O bonds with different bond energy on the surface of LaMn_4O_x [39]. In addition, the H_2 consumption amount for LaMn_4O_x was significantly greater than Mn_2O_3 , revealing the hierarchical perovskite structure of LaMn_4O_x facilitated the exposure of more reducible sites.

NH_3 -TPD was employed for qualitatively evaluating the amount of acid sites on the catalysts (Fig. 4B). The adsorption peak intensity for LaMn_4O_x was substantially greater than that of Mn_2O_3 , suggesting a higher amount of acid sites on the perovskite surface. Previous studies revealed that surface Lewis acid sites such as metal cations, surface hydroxyl groups and oxygen vacancies are essential for catalytic ozonation, since they were considered as the main adsorption sites for ozone molecules and the ion-exchange bridge for ozone decomposition to produce reactive species [36,40]. To differentiate the types of acids sites, pyridine FTIR was performed (Fig. 4C). IR bands centered around 1587 and 1440 cm^{-1} were discerned, which could be ascribed to pyridine adsorbed on Lewis acids sites. The peaks centered at 1540 and 1486 cm^{-1} was assigned to the pyridine adsorbed on strong Brønsted acid and both Lewis and Brønsted acid sites, respectively [28,36]. For both materials, the intensities of Lewis acid peaks were notably higher than those of Brønsted acid, suggesting Lewis acid was the main acid site responsible for catalytic decomposition of ozone on LaMn_4O_x and Mn_2O_3 . The trivial peaks observed in the spectra might be attributed to the unadsorbed free pyridine [28].

As one of the Lewis acidic sites, surface hydroxyl group has been reported as the potential active site in catalytic ozonation [34,36] and the concentration of which could be determined by TGA in N_2 atmosphere (Fig. 4D). The weight loss at the temperature ranges between 120 ~ 300 °C and 300 ~ 650 °C was assigned to weakly and strongly bonded surface hydroxyl groups, respectively [28]. Mn_2O_3 obtained a low concentration of surface hydroxyl group, and less than 0.5 wt% was identified. LMO perovskite composites displayed similar surface hydroxyl groups concentration (1 wt.%), suggesting that the incorporation of La could increase the surface hydroxyl groups and thus possibly contribute to the catalytic activity.

Average oxidation state (AOS) of Mn was calculated by following equation (Eq. (1)), where ΔE_s represents the energy difference between the two main peaks in Mn 3 s from XPS spectra (Fig. 5A) [41,42].

$$\text{AOS} = 8.95 - 1.13\Delta E_s \quad (1)$$

Listed in Table 1, the AOS of Mn for LaMn_4O_x was smaller than that of LaMnO_x (3.08 vs. 3.16), suggesting more Mn^{3+} was formed by the formation of the hierarchical structure, which corresponds to Mn 2p deconvolution results (Table S2 and Fig. S12). For LMO perovskites, decreasing the AOS of Mn also led to the formation of oxygen vacancies in B sites [42]. For the used LaMn_4O_x , the AOS of Mn increased to 3.23, suggesting the redox reactions occurred between $\text{Mn}^{3+}/\text{Mn}^{4+}$ pairs were critical in LMO perovskite-based catalytic ozonation. Furthermore, the partial filling of the oxygen vacancies by the oxidation reaction from ROS also contribute to the increase of AOS. XPS O1s surveys were deconvoluted to investigate the composition of the oxygen species (Fig. S13). The peaks centered at 529.3, 531.2 and 533.1 eV could be assigned to the lattice oxygen, OH groups/oxygen vacancies and adsorbed molecular water, respectively [43]. Compared with LaMnO_x , formation of hierarchical structure of LaMn_4O_x promote the evolution of the lattice oxygen to OH groups/oxygen vacancies.

O_2 -TPD was then employed to investigate the oxygen vacancy (Fig. S14). For LMO-based perovskites, the dominant peak centered around 290 °C was observed for all the samples, ascribing to the desorption of the oxygen chemically adsorbed on the oxygen vacancies [44]. The higher peak intensity of LaMn_4O_x than LaMnO_x suggested that increase

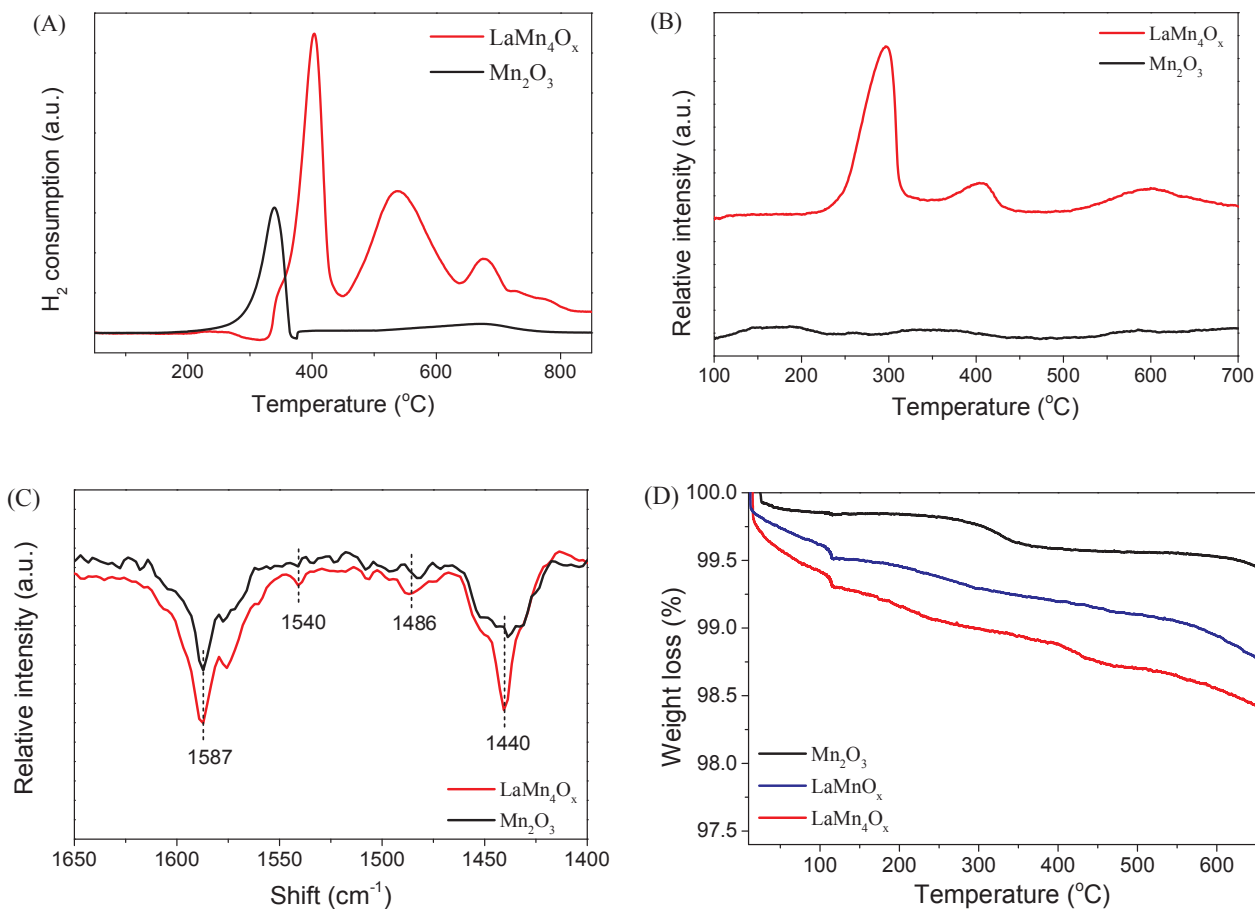


Fig. 4. (A) H₂-TPD profiles of LaMn₄O_x and Mn₂O₃; (B) NH₃-TPD profile of LaMn₄O_x and Mn₂O₃; (C) Pyridine adsorbed FTIR for Mn₂O₃ and LaMn₄O_x; (D) TGA analysis in N₂ atmosphere for evaluation of the concentration of surface hydroxyl groups.

the Mn/La ratio facilitated the formation of more oxygen vacancies. The decrease of the peak intensity of used-LaMn₄O_x might be ascribed to the partial filling of the oxygen vacancies through the surface oxidation process by ROS, which well explained the passivation of the activity. The absence of desorption peak at around 290 °C in Mn₂O₃ indicated the insignificant amount of oxygen vacancies were formed.

The oxygen vacancy content (δ value) of the LMO-based materials at room temperature was determined by the iodometric titration method [6,45]. The detailed illustration of iodometric titration can be found in Text S6 in supplementary data. The calculated δ values for Mn₂O₃,

LaMnO_x, LaMn₄O_x and used LaMn₄O_x were 0.03, 0.11, 0.13 and 0.08, respectively. The oxygen vacancy amounts were then correlated with pseudo-first order reaction rate constants for OA degradation of these catalysts (Fig. 5B). Higher amount of oxygen vacancy (δ value) led to a greater rate constant, revealing the crucial contribution of oxygen vacancy to the catalytic activity. Defective sites, especially oxygen vacancies on the surface of metal oxides, obtain a strong catalytic potential since they tailored the electronic structure by removing bonded oxygen atoms [9,19]. In catalytic ozonation processes, oxygen vacancies would act as the Lewis acid sites and facilitate the adsorption of

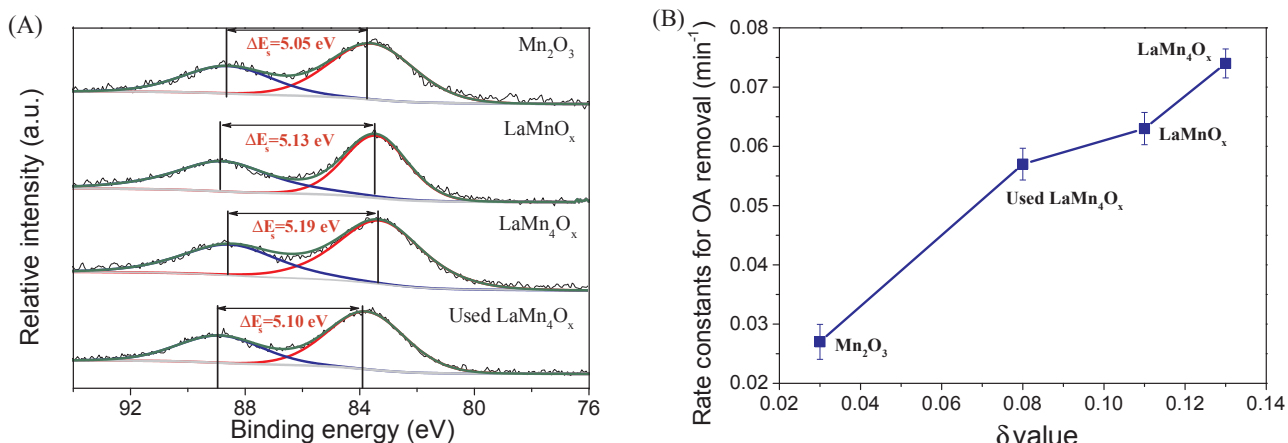


Fig. 5. (A) High-resolution XPS survey on Mn 3 s; (B) Correlation between pseudo-first order reaction rate constants for OA degradation and the oxygen vacancy amounts (δ values) of the catalysts.

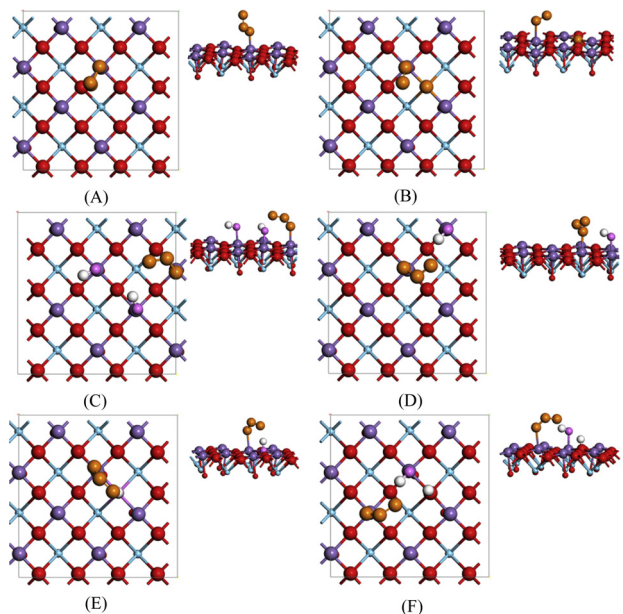


Fig. 6. DFT simulations of the favorable interaction between the ozone molecule and different sites on (001) surface of LaMnO_3 : Ozone adsorption on bare LaMnO_3 (001) surface (A); on oxygen vacancy of LaMnO_3 (001) surface (B); on hydrogen-bonded terminal OH group (C); on edge isolated terminal OH group (D); isolated OH group near oxygen vacancy (E); hydrogen-bonded OH group near oxygen vacancy (F). Color scheme: Blue: La; Purple: Mn; Red: O in LaMnO_3 ; White: H; Pink: O in OH; Orange: O in ozone. (For interpretation of the references to colour in this figure legend, the reader is referred to the web version of this article).

O_3 molecules by depriving their electrons. The resulted chemical bonds between Mn cations and O_3 would bring about the elongation of O–O bond within O_3 and thus accelerate the formation of ROS [19,46]. Apart from the oxygen vacancies on metal surfaces, our previous study also discovered the structural defects within graphene layers obtaining a high catalytic activity on O_3 dissociation [47]. Noted that the contribution of other surface Lewis acidic sites such as hydroxyl groups and Mn^{3+} sites to the catalytic activity might lead to linearity aberration of this correlation.

3.5. DFT simulation for ozone adsorption behavior on LMO perovskite's surface

To unveil the potential active sites and enable profound insights into the ozone decomposition on LMO perovskite's surface, DFT-based theoretical calculations were performed. A LaMnO_3 model was employed as the alternative of the identified $\text{LaMnO}_{3-\delta}$ for simplicity of modeling. The most stable Mn-terminated surface (010) with four layers was utilized for ozone adsorption [30,48]. Moreover, considering the minor composition of $\alpha\text{-Mn}_2\text{O}_3$ within the composite as well as its inferior catalytic activity, only LaMnO_3 model was taken into consideration. Fig. 6A describes the favorable adsorption behavior of the ozone molecule on the Mn-terminated (010) surface of LaMnO_3 . As seen, the single-bonded O atom prefers to form a weak covalent bond with the bond length ($l_{\text{Mn-O}}$) of 2.218 Å at the Mn site on perovskite's surface. The generated covalent bond would act as the bridge for transferring the electrons from Mn redox cycle to ozone. As a result, the length of O–O bond ($l_{\text{O-O}}$) in O_3 was significantly extended from 1.285 to 1.524 Å (Table S3). The stretched $l_{\text{O-O}}$ suggested that Mn sites on the LaMnO_3 surface exhibited catalytic potential for ozone decomposition. Compared with $l_{\text{Mn-O}}$ within LaMnO_3 structure (1.899 Å), the newly formed covalent bonds obtained a much longer $l_{\text{Mn-O}}$, indicating that the high tendency of dissociation to form ROS during the possible upcoming electron transfer process. Fig. 6B illustrates the influence of oxygen

vacancy on ozone adsorption. To simulate, one oxygen atom was removed from the LaMnO_3 crystal structure to mimic the oxygen vacancy (Fig. S15). Owing to the strong Lewis acidic property of oxygen vacancy, the O–O bond in ozone was spontaneously dissociated. The unbonded O atom occupied the vacancy while the remained moiety formed the weak Mn–O covalent bond ($l_{\text{Mn-O}} = 2.199$ Å), which provided the possibility for generation of ROS with two O atoms. The adsorption energies of ozone on Mn sites and oxygen vacancies were calculated to be -1.48 and -2.04 eV, respectively. The stronger adsorption energy suggested that oxygen vacancies within LaMnO_3 structure obtained more catalytic potential for ozone decomposition.

Catalytic potential of the surface hydroxyl groups on LMO for ozone dissociation was also investigated. Apart from the self-obtained OH groups on perovskite surface, hydroxyl groups would also arise from the hydroxylation occurring on the surface of metal oxides in aqueous solution and could be classified into the isolated (free) one and the hydrogen-bonded ones (Fig. S16) [49]. Fig. 6C–F demonstrate the ozone adsorption behavior on different configurations of surface hydroxyl groups (isolated and hydrogen bonded ones on Mn atom and oxygen vacancy). The single-bonded O atom from ozone molecule still preferred to bond with the Mn sites to form weak Mn–O covalent bonds rather than interacting with surface hydroxyl groups. Although the $l_{\text{O-O}}$ within the ozone structure was stretched in each configuration, the adsorption energy in OH-involved configurations was much inferior to those of Mn sites and oxygen vacancy (Table S3). Therefore, Mn sites and oxygen vacancies are favorable for electron transfer and act as the dominant catalytic sites for ozone decomposition to produce ROS. Particularly, the spontaneous ozone dissociation on oxygen vacancies are beneficial for ROS generation. The surface OH groups as the Lewis acid sites further contributed to the ozone activation by stretching the O–O bonds.

3.6. Probing the generated ROS for catalytic ozonation over BTA degradation

Competitive radical tests were performed to discover the effect of generated ROS on BTA degradation. $\cdot\text{OH}$ with the redox potential of 2.7 V has been recognized as one of the prevailing ROS produced during the catalytic ozonation process for organics decomposition [36]. t-BA has been employed as an effective $\cdot\text{OH}$ scavenger in catalytic ozonation reactions ($k_{\text{O}_3} = 3 \times 10^{-5} \text{ M}^{-1} \text{ s}^{-1}$, $k_{\cdot\text{OH}} = 3.8 \times 10^8$ – $7.6 \times 10^8 \text{ M}^{-1} \text{ s}^{-1}$) [34]. Interestingly, insignificant quenching effect on BTA degradation rate was observed with the addition of 10 mM of t-BA (Fig. 7A). Different from t-BA, bicarbonate anion (HCO_3^-) would bind with catalyst's surface and compete with the refractory organic pollutants for $\cdot\text{OH}$ consumption ($8.5 \times 10^6 \text{ M}^{-1} \text{ s}^{-1}$) [50,51]. As seen, HCO_3^- did quench BTA degradation and the corresponding TOC removal. A distinct decrease in TOC removal rate was observed (from 95% to 68%), suggesting $\cdot\text{OH}$ was generated and responsible for BTA decomposition. Since t-BA obtains low affinity towards the surface of catalyst, this trend indicated ozone decomposition for $\cdot\text{OH}$ generation might predominantly occur on catalyst surface, which consolidated DFT results. On the other hand, the emerged fine bubbles with the presence of t-BA would increase the overall mass transfer rate to enhance reaction rate. Nevertheless, increasing the HCO_3^- dosage to 600 mg/L would not give rise to a higher TOC removal rate (Fig. S17), indicating that other ROS apart from $\cdot\text{OH}$ might also contribute to the overall TOC removal. EPR signals for DMPO- $\cdot\text{OH}$ adducts are displayed in Fig. S18. Higher intensity of the DMPO- $\cdot\text{OH}$ peaks was observed for catalytic ozonation than in single ozonation, suggesting the generation of more $\cdot\text{OH}$.

Recently, superoxide radicals ($\text{O}_2^{\cdot-}$) has been suggested as one of crucial ROS generated in catalytic ozonation process [14,51]. Under a less acidic environment, $\text{O}_2^{\cdot-}$ would bind with the H^+ to form HO_2^{\cdot} [52]. $\text{HO}_2^{\cdot}/\text{O}_2^{\cdot-}$ not only acts as the pivotal role as the intermediate for $\cdot\text{OH}$ formation, but also obtains high affinity for destructing organic pollutants [53]. To investigate the generation of $\text{HO}_2^{\cdot}/\text{O}_2^{\cdot-}$ during

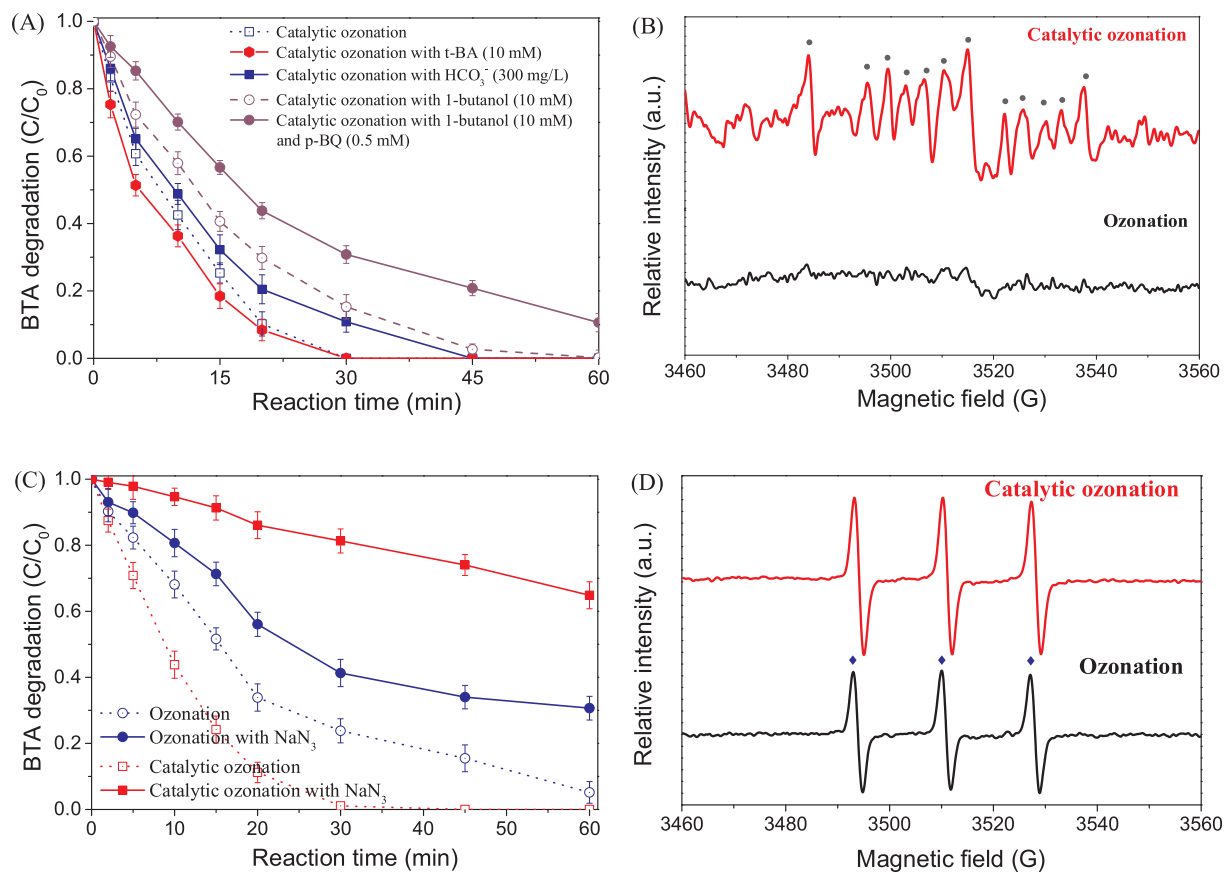


Fig. 7. (A) Effect of different radical scavengers on BTA degradation efficiency; (B) EPR spectra employing DMPO as the trapping agent with ultrapure water as reaction medium with methanol as reaction medium; (C) Effect of NaN₃ on BTA degradation efficiency at pH 3; (D) EPR spectra utilizing TEMP as the trapping agent with ultrapure water as reaction medium. Competitive radical tests condition: [BTA]₀: 50 mg/L; Catalyst loading: 0.2 g/L; Ozone concentration: 50 mg/L; Ozone flow rate: 100 mL/min; Temperature: 25 °C; [t-BA]: 10 mM; [HCO₃⁻]: 300 mg/L; [1-butanol]: 10 mM; [p-BQ]: 0.5 mM; [NaN₃]: 12 mM. EPR condition: Centerfield: 3510 G; Sweep width: 100 G; Microwave frequency: 9.87 GHz; Modulation frequency: 100 GHz; Power: 18.11 mW; Catalyst loading: 0.2 g/L, Ozone flow rate: 300 mL/min; Ozone loading: 50 mg/L; Temperature: 25 °C.

catalytic ozonation, EPR study employing DMPO as spin trapping agent was performed (Fig. 7B). With the addition of methanol as the ·OH scavenger, DMPO-OOH adducts with the hyperfine splitting constants of $a_N = 14.2$ G, $a_H^{\beta} = 11.4$ G, $a_H^{\gamma} = 1.2$ G were observed in catalytic ozonation processes [54,55]. On the contrary, DMPO-OOH was not detected in single ozonation in absence of the catalyst.

p-BQ has been widely employed as the superoxide radical scavenger ($k_{HO_2^-/O_2^-} = 3.5 \times 10^8 - 7.8 \times 10^8 \text{ M}^{-1}\text{s}^{-1}$) [56]. However, p-BQ also react with the generated ROS, especially ·OH ($k_{\cdot OH} = 1.2 \times 10^9 \text{ M}^{-1}\text{s}^{-1}$) [57] and ozone ($k_{O_3} = 2.5 \times 10^3 \text{ M}^{-1}\text{s}^{-1}$) [58], making the result less accurate. 1-Butanol obtained a 4-fold faster reaction rate constant with ·OH ($k_{\cdot OH} = 4.5 \times 10^9 \text{ M}^{-1}\text{s}^{-1}$) than p-BQ [57]. Addition of p-BQ with the presence of overdosed 1-butanol could screen the interference of ·OH to some extent. As seen, the presence of 10 mM of 1-butanol led to a slightly higher inhibition effect than HCO₃⁻. When p-BQ (0.5 mM) was also involved, the BTA degradation was further inhibited. Combined with the EPR evidence, we validated the effect of HO₂[·]/O₂^{·-} on BTA degradation owing to the much higher reaction rate of p-BQ with HO₂[·]/O₂^{·-} than with ozone.

Apart from ·OH and HO₂[·]/O₂^{·-}, singlet oxygen (¹O₂) obtaining the redox potential of 0.85 V has been suggested as another potential ROS generated during catalytic ozonation [53,59]. EPR tests utilizing 4-hydroxyl-2,2,6,6-tetramethyl-4-piperidine (TEMP) as the spin trapping agent were conducted (Fig. 7D). The characteristic triplet TEMPO signals revealed the production of ¹O₂ in ozonation, and the same TEMPO signals were also discerned in catalytic ozonation with higher intensities, suggesting a greater amount of ¹O₂ was generated. Although

judging the concentration of ROS by signal intensities might not be accurate, the signal intensity would be utilized to qualify the ROS generation trend. To evaluate the effect of ¹O₂ on BTA destruction, sodium azide (NaN₃) with a fast reaction rate constant of $2 \times 10^9 \text{ M}^{-1}\text{s}^{-1}$ was suggested as an efficient quenching agent toward ¹O₂ [60]. However, previous studies revealed that dissolved ozone would quickly deplete by reacting with NaN₃ in the neutral or alkaline pH, thus depriving the quenching effect of NaN₃ to ¹O₂ [61,62]. Under the acidic pH environment, the reaction between ozone and NaN₃ was significantly suppressed [63].

In acidic solution (initial pH 3), control experiments revealed that only part of ozone molecules was consumed by azide (12 mM), revealing the relatively sluggish reaction rate between ozone and azide (Fig. S19). For catalytic ozonation, 65% of BTA remained with the presence of NaN₃ (Fig. 7C). TOC removal rate was suppressed from 60% to 10%. It is worth noting that NaN₃ has also been reported as an efficient hydroxyl radical scavenger with a rate constant of $1 \times 10^9 \text{ M}^{-1}\text{s}^{-1}$ [54]. Therefore, considering the contribution of ·OH proven by the addition of HCO₃⁻, the quenching effect brought by the addition of NaN₃ could be ascribed to the combined results of both ·OH and ¹O₂.





We proposed the possible radical generation mechanism based on the results of both experimental and theoretical studies. The DFT calculation suggested the O_3 molecule would catalytically decompose into the surface adsorbed atomic oxygen (O_{ad}^*) and the free peroxide (${}^*\text{O}_2$) on the active sites (Eq. (2)). The O_{ad}^* would be protonated by the ambient water molecules and desorbed from the catalyst's surface to form $\cdot\text{OH}$, which is not only responsible for destruction of BTA molecules (Eq. (3)), but also would induce the further radical chain reaction. With electron transfer process by the ambient water molecules, ${}^*\text{O}_2$ might be transformed to $\text{HO}_2^- / \text{O}_2^-$ which would either attack BTA (Eq. (4)) or further react with O_3 to form $\cdot\text{OH}$ (Eq. (5)). Moreover, the formation of ${}^1\text{O}_2$ might possibly arise from this ${}^*\text{O}_2$ and responsible for BTA degradation (Eq. (6)).

4. Conclusions

In summary, hierarchical $\text{Mn}_2\text{O}_3 / \text{LaMnO}_{3-\delta}$ composites were synthesized via a facile co-precipitation method for catalytic ozonation of OA and BTA. The degradation results, AOS study based on XPS analysis and TPD/TPR results suggested that oxygen vacancies, the $\text{Mn}^{3+}/\text{Mn}^{4+}$ redox centers and the surface hydroxyl groups were the potential active sites for ozone decomposition. DFT simulations further revealed that ozone would be spontaneously dissociated on oxygen vacancy to produce double-oxygen species, while Mn sites and surface hydroxyl groups facilitated ozone dissociation by stretching the O–O bonds. Radical scavenging tests and EPR analysis indicated that apart from $\cdot\text{OH}$, O_2^- and ${}^1\text{O}_2$ also contributed to BTA degradation in LaMnO_4 _x catalytic ozonation. The produced O_2^- and ${}^1\text{O}_2$ might originate from the ozone dissociated products on oxygen vacancies while $\cdot\text{OH}$ might be stemmed from O_3 adsorbed on Mn sites and/or surface hydroxyl groups.

Conflicts of interest

There are no conflicts to declare.

Acknowledgements

The authors greatly appreciate the financial supports from the National Natural Science Foundation of China (No. 21606253), the National Science Fund for Distinguished Young Scholars of China (No. 51425405), Science Foundation of China University of Petroleum, Beijing (No. 2462016YJRC013), Beijing Natural Science Foundation (8172043) and Major Science and Technology Program for Water Pollution Control and Treatment (2017ZX07402003, 2017ZX07402001).

Appendix A. Supplementary data

Supplementary material related to this article can be found, in the online version, at doi:<https://doi.org/10.1016/j.apcatb.2019.01.025>.

References

- [1] J.T. Mefford, X. Rong, A.M. Abakumov, W.G. Hardin, S. Dai, A.M. Kolpak, K.P. Johnston, K.J. Stevenson, *Nat. Commun.* 7 (2016) 11053.
- [2] H. Zhu, P. Zhang, S. Dai, *ACS Catal.* 5 (2015) 6370–6385.
- [3] M.H. Seo, H.W. Park, D.U. Lee, M.G. Park, Z. Chen, *ACS Catal.* 5 (2015) 4337–4344.
- [4] B. Saparov, D.B. Mitzi, *Chem. Rev.* 116 (2016) 4558–4596.
- [5] X. Duan, C. Su, J. Miao, Y. Zhong, Z. Shao, S. Wang, H. Sun, *Appl. Catal. B* 220 (2018) 626–634.
- [6] J.T. Mefford, W.G. Hardin, S. Dai, K.P. Johnston, K.J. Stevenson, *Nat. Mater.* 13 (2014) 726.
- [7] D.N. Mueller, M.L. Machala, H. Bluhm, W.C. Chueh, *Nat. Commun.* 6 (2015) 6097.
- [8] S. Gong, Z. Xie, W. Li, X. Wu, N. Han, Y. Chen, *Appl. Catal. B* 241 (2019) 578–587.
- [9] Q. Zhang, Y. Huang, S. Peng, T. Huang, J. Cao, W. Ho, S. Lee, *Appl. Catal. B* 239 (2018) 1–9.
- [10] A. Vojvodic, J.K. Nørskov, *Science* 334 (2011) 1355.
- [11] X. Ge, Y. Du, B. Li, T.S.A. Hor, M. Sindoro, Y. Zong, H. Zhang, Z. Liu, *ACS Catal.* 6 (2016) 7865–7871.
- [12] E. Saputra, S. Muhammad, H. Sun, H.-M. Ang, M.O. Tadé, S. Wang, *Appl. Catal. B* 154–155 (2014) 246–251.
- [13] A.G. Bhavani, W.Y. Kim, J.S. Lee, *ACS Catal.* 3 (2013) 1537–1544.
- [14] Y. Wang, Y. Xie, H. Sun, J. Xiao, H. Cao, S. Wang, *Catal. Sci. Technol.* 6 (2016) 2918–2929.
- [15] J. Sunarso, A.A.J. Torriero, W. Zhou, P.C. Howlett, M. Forsyth, *J. Phys. Chem. C* 116 (2012) 5827–5834.
- [16] K.A. Stoerzinger, M. Risch, J. Suntivich, W.M. Lu, J. Zhou, M.D. Biegalski, H.M. Christen, Ariando, T. Venkatesan, Y. Shao-Horn, *Energy Environ. Sci.* 6 (2013) 1582–1588.
- [17] T.Y. Ma, Y. Zheng, S. Dai, M. Jaroniec, S.Z. Qiao, *J. Mater. Chem. A* 2 (2014) 8676–8682.
- [18] F. Fang, N. Feng, L. Wang, J. Meng, G. Liu, P. Zhao, P. Gao, J. Ding, H. Wan, G. Guan, *Appl. Catal. B* 236 (2018) 184–194.
- [19] G. Zhu, J. Zhu, W. Jiang, Z. Zhang, J. Wang, Y. Zhu, Q. Zhang, *Appl. Catal. B* 209 (2017) 729–737.
- [20] E. Borowska, E. Felis, J. Kalka, *Chem. Eng. J.* 304 (2016) 852–863.
- [21] E. Felis, A. Sochacki, S. Magiera, *Water Res.* 104 (2016) 441–448.
- [22] Y. Wang, H. Sun, X. Duan, H.M. Ang, M.O. Tadé, S. Wang, *Appl. Catal. B* 172–173 (2015) 73–81.
- [23] H. Xu, D. Wang, J. Ma, T. Zhang, X. Lu, Z. Chen, *Appl. Catal. B* 238 (2018) 557–567.
- [24] B. Kasprzyk-Hordern, M. Ziolk, J. Nawrocki, *Appl. Catal. B* 46 (2003) 639–669.
- [25] J. Nawrocki, B. Kasprzyk-Hordern, *Appl. Catal. B* 99 (2010) 27–42.
- [26] H. Cao, L. Xing, G. Wu, Y. Xie, S. Shi, Y. Zhang, D. Minakata, J.C. Crittenden, *Appl. Catal. B* 146 (2014) 169–176.
- [27] S. Saeid, P. Tolvanen, N. Kumar, K. Eränen, J. Peltonen, M. Peurla, J.-P. Mikkola, A. Franz, T. Salmi, *Appl. Catal. B* 230 (2018) 77–90.
- [28] S. Afzal, X. Quan, J. Zhang, *Appl. Catal., B* 206 (2017) 692–703.
- [29] S.B. Hammouda, C. Salazar, F. Zhao, D.L. Ramasamy, E. Laklova, S. Iftekhar, I. Babu, M. Sillanpää, *Appl. Catal. B* 240 (2019) 201–214.
- [30] C.R. Billman, Y. Wang, H. Cheng, *J. Chem. Phys.* 144 (2016) 064701.
- [31] A. Machocki, T. Ioannides, B. Stasinska, W. Gac, G. Avgouropoulos, D. Delimaris, W. Grzegorczyk, S. Pasieczna, *J. Catal.* 227 (2004) 282–296.
- [32] X. Han, T. Zhang, J. Du, F. Cheng, J. Chen, *Chem. Sci.* 4 (2013) 368–376.
- [33] D.S. Pines, D.A. Reckhow, *Environ. Sci. Technol.* 36 (2002) 4046–4051.
- [34] A. Lv, C. Hu, Y. Nie, J. Qu, *Appl. Catal. B* 117 (2012) 246–252.
- [35] J. Bing, C. Hu, L. Zhang, *Appl. Catal. B* 202 (2017) 118–126.
- [36] J. Bing, C. Hu, Y. Nie, M. Yang, J. Qu, *Environ. Sci. Technol.* 49 (2015) 1690–1697.
- [37] F. Nawaz, Y. Xie, H. Cao, J. Xiao, Yueqiu Wang, X. Zhang, M. Li, F. Duan, *Catal. Today* 258 (2015) 595–601.
- [38] Y. Liu, H. Dai, Y. Du, J. Deng, L. Zhang, Z. Zhao, C.T. Au, *J. Catal.* 287 (2012) 149–160.
- [39] V.P. Santos, M.F.R. Pereira, J.J.M. Órfão, J.L. Figueiredo, *Appl. Catal. B* 99 (2010) 353–363.
- [40] S.S. Sable, P.P. Ghute, D. Fakhrnasova, R.B. Mane, C.V. Rode, F. Medina, S. Contreras, *Appl. Catal. B* 209 (2017) 523–529.
- [41] V.P. Santos, O.S.G.P. Soares, J.J.W. Bakker, M.F.R. Pereira, J.J.M. Órfão, J. Gascon, F. Kapteijn, J.L. Figueiredo, *J. Catal.* 293 (2012) 165–174.
- [42] J. Hou, Y. Li, M. Mao, L. Ren, X. Zhao, *ACS Appl. Mater. Interfaces* 6 (2014) 14981–14987.
- [43] K. Jirátová, J. Mikulová, J. Klempa, T. Grygar, Z. Bastl, F. Kovanda, *Appl. Catal. A* Gen. 361 (2009) 106–116.
- [44] Z. Zhao, X. Yang, Y. Wu, *Appl. Catal. B* 8 (1996) 281–297.
- [45] R. Laiho, K. Lisunov, E. Lähderanta, P. Petrenko, J. Salminen, V. Stamov, Y.P. Stepanov, V. Zakhvalinskii, *J. Phys. Chem. Solids* 64 (2003) 2313–2319.
- [46] J. Ma, C. Wang, H. He, *Appl. Catal. B* 201 (2017) 503–510.
- [47] Y. Wang, H. Cao, L. Chen, C. Chen, X. Duan, Y. Xie, W. Song, H. Sun, S. Wang, *Appl. Catal. B* 229 (2018) 71–80.
- [48] Y. Wang, H. Cheng, *J. Phys. Chem. C* 117 (2013) 2106–2112.
- [49] H. Tamura, K. Mita, A. Tanaka, M. Ito, *J. Colloid Interface Sci.* 243 (2001) 202–207.
- [50] J. Ma, N.J.D. Graham, *Water Res.* 34 (2000) 3822–3828.
- [51] J.L. Acero, Uv. Gunten, *Ozone Sci. Eng.* 22 (2000) 305–328.
- [52] D. Behar, G. Czapski, J. Rabani, L.M. Dorfman, H.A. Schwarz, *J. Phys. Chem.* 74 (1970) 3209–3213.
- [53] X. Duan, Z. Ao, H. Sun, S. Indrawirawan, Y. Wang, J. Kang, F. Liang, Z.H. Zhu, S. Wang, *ACS Appl. Mater. Interfaces* 7 (2015) 4169–4178.
- [54] J. Catalán, C. Diaz, L. Barrio, *Chem. Phys.* 300 (2004) 33–39.
- [55] S. Inoue, S. Kawanishi, *Biochem. Biophys. Res. Commun.* 159 (1989) 445–451.
- [56] R.I. Samoilova, A.R. Crofts, S.A. Dikanov, *J. Phys. Chem. A* 115 (2011) 11589–11593.
- [57] G.V. Buxton, C.L. Greenstock, W.P. Helman, A.B. Ross, *J. Phys. Chem. Ref. Data* 17 (1988) 513–886.
- [58] P.R. Tentscher, M. Bourgin, U. von Gunten, *Environ. Sci. Technol.* 52 (2018) 4763–4773.
- [59] Y. Wang, Y. Xie, H. Sun, J. Xiao, H. Cao, S. Wang, *ACS Appl. Mater. Interfaces* 8 (2016) 9710–9720.
- [60] A. Jawad, X. Lu, Z. Chen, G. Yin, *J. Phys. Chem. A* 118 (2014) 10028–10035.
- [61] D.B. Mawhinney, B.J. Vanderford, S.A. Snyder, *Environ. Sci. Technol.* 46 (2012) 7102–7111.
- [62] F.J. Benítez, J.L. Acero, F.J. Real, G. Roldán, E. Rodríguez, *J. Hazard. Mater.* 282 (2015) 224–232.
- [63] E.A. Betterton, D. Craig, *J. Air Waste Manage. Assoc.* 49 (1999) 1347–1354.